Materials Advances

ROYAL SOCIETY OF CHEMISTRY

PAPER

View Article Online
View Journal

Cite this: DOI: 10.1039/d6ma00157b

First-principles design of a lead-free $Cs_2LiFeCl_6$ double perovskite for solar-driven hydrogen evolution and CO_2 reduction

Md. Jahidul Islam, †[ac] Mahbub Alam Rabin †[b] and Fahmida Gulshan *[c]

The development of lead-free, stable, and earth-abundant materials for solar energy conversion remains a critical challenge for next-generation photovoltaics and photocatalysis. Herein, we present a comprehensive first-principles investigation of the cesium-based transition-metal double perovskite $Cs_2LiFeCl_6$ using density functional theory with an on-site Hubbard correction. The compound crystallizes in a cubic elpasolite structure, supported by favorable Goldschmidt (1.038) and one-dimensional (2.205) tolerance factors. Thermodynamic stability is confirmed by a negative formation energy and a positive decomposition energy, while phonon dispersion calculations reveal the absence of imaginary modes, establishing dynamic stability. Mechanical analysis shows compliance with Born stability criteria and a ductile nature, with a Pugh's ratio of 1.81 and a Poisson's ratio of 0.27, indicative of predominantly ionic bonding. Spin-polarized electronic structure calculations reveal a semiconducting ground state with a Hubbard-corrected band gap of 1.578 eV, where both the valence and conduction band edges are dominated by the spin-down channel arising from Fe-3d and Cl-3p hybridization. Importantly, band-edge alignment relative to the vacuum level demonstrates that $Cs_2LiFeCl_6$ satisfies the energetic requirements for photocatalytic hydrogen evolution over a broad pH range and shows favorable band-edge alignment for photocatalytic CO_2 reduction half-reactions associated with CH_3OH and CH_4 production. These combined structural robustness, favorable optoelectronic characteristics, and dual photocatalytic functionality establish $Cs_2LiFeCl_6$ as a promising lead-free platform for integrated solar-to-fuel and photocatalytic energy-conversion applications.

Received 2nd February 2026,
Accepted 8th June 2026

DOI: 10.1039/d6ma00157b

rsc.li/materials-advances

1 Introduction

The growing global demand for energy has significantly increased the consumption of fossil fuels, leading to environmental pollution and global warming. To address these challenges, sustainable energy solutions have become a global priority. Silicon-based solar cells have played a central role in renewable energy technologies; however, their limited efficiency and complex fabrication processes have driven the search for alternative photovoltaic (PV) materials that are both efficient and cost-effective.[1] Among these alternatives, lead halide perovskites have emerged as highly promising candidates due to their exceptional optical and electronic properties, tunable bandgaps, high absorption coefficients, and efficient charge transport mechanisms.[2] These materials have rapidly advanced in the field of photovoltaics, achieving a certified power conversion efficiency (PCE) of up to 26.7% in single-junction devices.[3] Beyond solar cells, lead halide perovskites are also being explored in optoelectronic applications such as lasers,[4] detectors,[5,6] transistors,[7] and photocatalysts.[8] Despite their performance advantages, their practical deployment faces challenges due to poor long-term stability, particularly under exposure to moisture and light and the toxic nature of lead, which is highly bioavailable and poses environmental and health risks.[9,10]

In response, research has shifted toward discovering more stable and environmentally benign alternatives. Recent advances in halide perovskite research have increasingly emphasized cesium-based lead-free double perovskites owing to their high synthesizability, phase stability, and environmentally benign composition. These materials typically adopt elpasolite-derived $A_2BB'X_6$ frameworks, in which the ordered B/B′-site arrangement allows toxic Pb^{2+} to be replaced by suitable monovalent and trivalent cations while maintaining charge neutrality.[2,11–13] This ordered framework is important

[a] Department of Materials and Metallurgical Engineering, Dhaka University of Engineering and Technology (DUET), Gazipur, Bangladesh
[b] Department of Nanomaterials and Ceramic Engineering, Bangladesh University of Engineering and Technology (BUET), Dhaka, Bangladesh
[c] Department of Materials and Metallurgical Engineering, Bangladesh University of Engineering and Technology (BUET), Dhaka, Bangladesh.
E-mail: fahmidagulshan@mme.buet.ac.bd
† Co-first authors.

because it can improve structural and chemical stability and enables electronic-structure tuning through distinct cation–anion interactions.[2,14,15] In Fe^{3+}-containing systems, the ordered octahedral environment further influences crystal-field splitting, magnetic interactions, and localized Fe-3d states, which are relevant for multifunctional applications.[16,17]

For cesium-based lead-free double perovskites, the general formula can be written as $Cs_2M^IM^{III}X_6$, where ionic-radius compatibility between the monovalent and trivalent cations plays a decisive role in phase formation and structural symmetry. Early crystallographic investigations on chloride elpasolites $Cs_2LiM^{3+}Cl_6$ established that the successful synthesis and stable crystallization of these compounds are primarily governed by the ionic radius of the trivalent metal cation.[18] In particular, compounds containing smaller trivalent cations such as Cr^{3+}, exemplified by the experimentally reported $Cs_2LiCrCl_6$, were shown to preferentially adopt hexagonal elpasolite-derived two-layer-type structures, indicating a radius-controlled structure-selection mechanism rather than intrinsic instability. The absence of reported decomposition or polymorphic instability for $Cs_2LiCrCl_6$ further confirms that such hexagonal phases are thermodynamically viable and synthetically accessible within the Li based cesium double perovskite family. In parallel, first-principles investigations have explored diverse combinations involving alkali metals (Li, Na, K, Cs), trivalent cations (In, Sc, V, Fe, Cu, Ga), and halogens (Cl, Br), targeting materials with favorable band gap characteristics, excellent carrier mobility, and high chemical stability,[19–22] thereby providing a robust theoretical framework for extending this structurally stable compositional space to other d block containing cesium double perovskites.

Building on this structurally stable and synthetically accessible foundation, cesium based double perovskites have demonstrated increasing relevance in solar energy driven applications spanning photovoltaics and photocatalysis. Representative systems such as $Cs_2AgBiBr_6$ exhibit high crystallinity, long carrier lifetimes, and strong environmental stability, with band gap tunability upon hydrogenation reaching values as low as 1.64 eV and photovoltaic efficiencies on the order of several percent.[23–26] Beyond photovoltaic operation, cesium double perovskites have shown notable activity toward photocatalytic hydrogen evolution and carbon dioxide reduction. For instance, $Cs_2AgBiBr_6$ based composites achieve near quantitative selectivity toward carbon monoxide formation under visible light, while $Cs_2NaBiBr_6$ displays a low activation barrier of approximately 0.67 eV with pronounced facet dependent activity.[27,28] Related compounds such as $Cs_2NaBiCl_6$ further combine favorable optical and thermoelectric properties with robust mechanical stability, and copper doped $Cs_2AgSbCl_6$ microcrystals have been experimentally demonstrated as efficient photocatalysts for carbon dioxide reduction.[29–31] Recent DFT studies on lead-free halide double perovskites such as Cs_3SbX_6 (X = F, Cl) have also reported promising structural stability and optoelectronic properties for scintillating and energy-related applications.[32] Collectively, these results highlight the versatility of cesium based double perovskites as stable and multifunctional platforms for solar energy conversion.

Cesium double perovskites incorporating transition metal cations have attracted growing attention due to their ability to exhibit coupled magnetic, electronic, and optoelectronic functionalities. Representative systems such as $Cs_2AgT^{3+}Cl_6$ with T = Fe and Cr,[33,34] $Cs_2NaT^{3+}Cl_6$ with T = Fe V Mn and Ni,[35,36] and $Cs_2KT^{3+}Cl_6$ with T = Mn Co and Ni[37] exhibit diverse magnetic ordering and spin mediated electronic behavior. The hexagonal $Cs_2AgCrCl_6$, synthesized in a paramagnetic phase, demonstrates favorable optoelectronic characteristics, highlighting the role of magnetic B site cations in tuning electronic structure, while cubic $Cs_2AgFeCl_6$ has shown encouraging photovoltaic performance.[33] More recently, $Cs_2NaFeCl_6$ has been synthesized as a thermally stable single crystal exhibiting reversible thermochromism from light yellow to black over the temperature range of 10 to 423 K.[38] Foundational structural studies on chloride elpasolites $Cs_2LiM^{3+}Cl_6$ established that crystal symmetry and phase stability are primarily dictated by the ionic radius of the trivalent metal cation.[18] Complementary first principles investigations on $Cs_2LiGaBr_6$ and $Cs_2NaGaBr_6$ predict visible light band gaps near 1.8 eV, strong electron phonon interactions, high optical absorption, and thermoelectric figures of merit exceeding unity, reinforcing their suitability for integrated energy conversion and solar fuel related technologies.[39]

In light of the above literature, we primarily focus on the cesium-based transition metal family of halide DPs, where an amalgamation of structural, electronic, mechanical and optoelectronic properties is discussed towards photocatalytic applications. With that perspective, we studied $Cs_2LiFeCl_6$ and it features a unique pairing of lightweight Li^+ and earth-abundant Fe^{3+} cations within the elpasolite-type framework. It offers potential advantages in terms of environmental safety, cost-effectiveness, and lattice tunability. Fe^{3+}-based halide perovskites such as $Cs_2NaFeCl_6$ have already demonstrated promising functional characteristics, including reversible thermochromism and high thermal stability over wide temperature ranges. The replacement of Na^+ with the smaller Li^+ ion in $Cs_2LiFeCl_6$ introduces additional structural compression and localized distortions, which are expected to influence both its electronic band structure and charge transport behavior. To investigate these effects, we performed a comprehensive DFT-based analysis to assess the crystal stability, mechanical robustness, electronic band dispersion, and carrier effective masses of $Cs_2LiFeCl_6$. Through this work, our objective is to position $Cs_2LiFeCl_6$ as a stable, efficient, and environmentally responsible candidate for future energy-related optoelectronic devices.

2 Computational methodology

In this study, first-principles calculations based on Density Functional Theory (DFT) are performed using the Vienna *ab initio* simulation package (VASP). The interactions between valence electrons and frozen core ions are described using the projector-augmented wave (PAW) method as implemented in VASP. The valence electron configurations considered for the constituent elements are as follows: Cs ($5s^2\ 5p^6\ 6s^1$), Li ($2s^1$), Fe

($3d^6\ 4s^2$), and Cl ($3s^2\ 3p^5$). The exchange–correlation functional is treated within the framework of the Generalized Gradient Approximation (GGA). To account for the strong correlation of Fe-3d electrons, the GGA+*U* approach was employed. The on-site Hubbard correction for the Fe-3d states was treated within the Dudarev GGA+*U* formalism using U_{eff} = 3 eV. The value of U_{eff} = 3 eV was selected based on previous DFT+*U* studies of Fe-containing halide double perovskites and related Fe-based perovskite systems, where similar values were used to describe localized Fe-3d states and spin-resolved electronic structures.[17,40,41]

All calculations were performed using a ferromagnetic (FM) spin-polarized configuration. The initial magnetic moment was set to $5\mu_B$ per Fe atom, while the remaining atoms were initialized with $0\mu_B$. A plane-wave cutoff energy of 600 eV is employed throughout all calculations. The Brillouin zone is sampled using the Monkhorst–Pack scheme, with a 6 × 6 × 6 *k*-point mesh for structural relaxation and geometry optimization, and a denser 9 × 9 × 9 mesh for electronic, magnetic, mechanical, and other property evaluations. Geometry optimization is carried out until the residual force on each atom is less than 0.005 eV $Å^{-1}$ and the total energy change between successive steps is below 10^{-8} eV. Phonon properties are calculated using density functional perturbation theory (DFPT) as implemented in VASP, interfaced with the Phonopy package for post-processing.

3 Results and discussion

3.1 Crystallographic structure

The geometry-optimized conventional unit cell of $Cs_2LiFeCl_6$ was calculated within the GGA framework.[42] The results confirm a cubic phase with the space group $Fm\bar{3}m$ (No. 225), consistent with the archetypal elpasolite structure of $A_2M^IM^{III}X_6$ double halide perovskites. During structural optimization, both the lattice structures and ionic positions were fully relaxed under stringent convergence criteria to ensure minimal total energy. As depicted in Fig. 1, the optimized structure positions Cs^+ ions at the 8c Wyckoff site, Fe^{3+} at the 4a site, Li^+ at the 4b site, and Cl^- at the 24e site with fractional coordinates. This configuration results in a three-dimensional framework of corner-sharing $FeCl_6$ and $LiCl_6$ octahedra, where each Fe^{3+} and Li^+ is octahedrally coordinated by six Cl^- anions. The disparity in ionic radii and valence states between Fe^{3+} and Li^+ leads to differing Fe–Cl and Li–Cl bond lengths, producing two distinct octahedral units that induce local distortions while preserving the global cubic symmetry.

The density functional theory calculations yield a lattice constant of 10.01 Å for $Cs_2LiFeCl_6$, consistent with a stable cubic elpasolite framework. The optimized structure exhibits distinct Fe–Cl and Li–Cl bond lengths of 2.39 Å and 2.62 Å, respectively, reflecting the difference in ionic radii and oxidation states of the hetero-occupied B-site cations. The Fe–Cl–Li bond angle remains 180°, confirming the absence of octahedral tilting and indicating ideal corner-sharing connectivity between adjacent $FeCl_6$ and $LiCl_6$ octahedra. Furthermore, the calculated octahedral edge lengths are 3.380 Å for Fe-centered octahedra and 3.698 Å for Li-centered octahedra, highlighting subtle local distortions while preserving the global cubic symmetry. This architectural arrangement significantly influences the optoelectronic behavior of the material, as the placement of hetero-charged B-site cations modulates bonding interactions and energy dispersion, thereby impacting key properties such as band gap and carrier mobility. Recent studies have demonstrated that tuning B-site cation ordering can further enhance optical performance in lead-free double perovskites.[26]

3.2 Structural and thermodynamic stability

To ensure that the cubic structure of the $Cs_2LiFeCl_6$ halide perovskite remains stable and free from distortions, two key parameters were used to assess its structural stability: the Goldschmidt tolerance factor (t)[43] and the one-dimensional tolerance factor (τ).[44] The Goldschmidt tolerance factor helps evaluate the size compatibility between ions in $A_2M^IM^{III}X_6$ perovskite. These are calculated as follows:

$$t = \frac{R_A + R_X}{\sqrt{2}\{R_M + R_X\}} \quad (1)$$

$$\tau = \frac{R_X}{R_M} - n_A\left(n_A - \frac{\frac{R_A}{R_M}}{\ln\left(\frac{R_A}{R_M}\right)}\right) \quad (2)$$

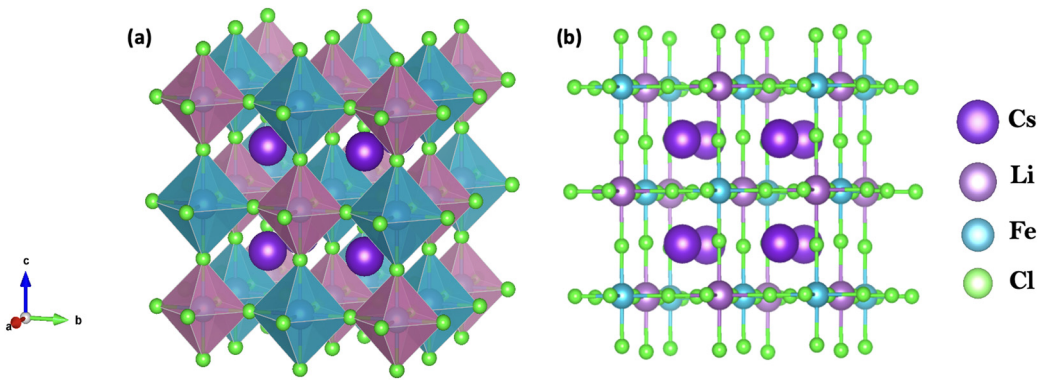

Fig. 1 Schematic representation of the crystal structure of $Cs_2LiFeCl_6$: (a) perspective view of the crystal lattice and (b) corresponding ball-and-stick model highlighting the atomic arrangement.

$$R_M = \frac{R_{M(I)} + R_{M(III)}}{2} \quad (3)$$

The one-dimensional tolerance factor, τ, was used as a complementary descriptor to the conventional Goldschmidt tolerance factor. While t mainly evaluates the size compatibility between the A-site cation and the corner-sharing octahedral network, τ additionally considers the A-site cation radius, the average octahedral-site cation radius, the anion radius, and the oxidation state of the A-site ion. Therefore, τ provides further insight into whether the ionic size distribution can support a stable three-dimensional perovskite framework. Here, R_A, $R_{M(I)}$, $R_{M(III)}$, and R_X refer to the effective ionic radii of the ions A, M^I, M^{III}, and X, based on Shannon's values,[45] and n_A represents the oxidation state of A. A good cubic structure is generally observed when the Goldschmidt factor (t) falls between 0.80 and 1.1. Values lower than this range can reduce symmetry and shift the structure from cubic to tetragonal or orthorhombic. On the other hand, higher values may cause distortion and lead to layered or non-ideal configurations. For the one-dimensional tolerance factor, $\tau < 4.18$ is generally associated with favorable perovskite formability. This new descriptor is said to achieve an accuracy of 91% for halide perovskites. The specific ionic radii values used in these calculations, based on the oxidation state and the coordination number from the DFT results, are listed in Table 1.The results show that both the Goldschmidt factor (1.038) and the one-dimensional tolerance factor (2.205) are within the stability range, indicating that $Cs_2LiFeCl_6$ is structurally stable and favors a 3D corner-sharing perovskite network without distortion.

To further evaluate the thermodynamic stability of $Cs_2LiFeCl_6$, the formation energy and decomposition energy were calculated. The formation energy per atom at 0 K was obtained as

$$E_F = \frac{1}{10}\left[E_{Cs_2LiFeCl_6} - (2E_{Cs} + E_{Li} + E_{Fe} + 6E_{Cl})\right], \quad (4)$$

where $E_{Cs_2LiFeCl_6}$ is the total energy of $Cs_2LiFeCl_6$, and E_{Cs}, E_{Li}, E_{Fe}, and E_{Cl} are the reference energies of the constituent elements. The calculated formation energy is −3.834 eV per atom, indicating that the formation of $Cs_2LiFeCl_6$ from its elemental constituents is energetically favorable.

The resistance of $Cs_2LiFeCl_6$ against decomposition was further examined by considering several chemically plausible competing pathways involving binary, ternary, mixed chloride, and elemental products. For each pathway, the decomposition energy was calculated as

$$E_{decomp} = \frac{1}{10}\left[\sum_i n_i E_i - E_{Cs_2LiFeCl_6}\right], \quad (5)$$

where E_i is the total energy of the i-th decomposition product and n_i is its stoichiometric coefficient in the balanced decomposition reaction. According to this definition, a positive E_{decomp} indicates that decomposition into the selected products is energetically unfavorable.

As summarized in Table 2, all considered decomposition pathways exhibit positive decomposition energies, ranging from +1.978 to +3.834 eV per atom. Among these pathways, the lowest decomposition energy is obtained for the reaction $Cs_2LiFeCl_6 \rightarrow CsFeCl_4 + CsLiCl_2$, with E_{decomp} = +1.978 eV per atom. Even this lowest-energy decomposition channel remains energetically unfavorable, supporting the thermodynamic stability of $Cs_2LiFeCl_6$ within the considered competing phase space.

Table 1 Shannon's effective ionic radii of the different elements in $Cs_2LiFeCl_6$

Element	Ionic state	Coordination number	Ionic radius (pm)
Cs	+1	12	188
Li	+1	6	76
Fe	+3	6	64.5
Cl	−1	6	181

Table 2 Calculated decomposition products and decomposition energies for $Cs_2LiFeCl_6$

No.	Decomposition products	E_{decomp} (eV per atom)
1	$2CsCl + FeCl_3 + LiCl$	+2.098
2	$CsFeCl_4 + CsCl + LiCl$	+1.991
3	$\frac{1}{3}Cs_3Fe_2Cl_9 + \frac{1}{3}FeCl_3 + CsCl + LiCl$	+2.034
4	$LiFeCl_4 + 2CsCl$	+2.053
5	$CsFeCl_4 + CsLiCl_2$	+1.978
6	$\frac{1}{2}Cs_3Fe_2Cl_9 + \frac{1}{2}CsLiCl_2 + \frac{1}{2}LiCl$	+1.996
7	$\frac{1}{2}Cs_3Fe_2Cl_9 + \frac{1}{2}CsLi_2Cl_3$	+1.993
8	$\frac{1}{2}Cs_3Fe_2Cl_9 + \frac{1}{2}CsCl + LiCl$	+2.002
9	2Cs + Li + Fe + 6Cl	+3.834

3.3 Dynamical stability

To further validate the structural robustness of the proposed perovskite, its dynamic stability was also examined. From the phonon band structures and DOS illustrated in Fig. 2, it is apparent that the $Fm\bar{3}m$ structure of $Cs_2LiFeCl_6$ is dynamically stable. This conclusion holds regardless of the computational details or cell type used. Our claim is based on the fact that there is no soft phonon mode (negative frequency) associated with either the acoustic or optical branches at the zone center or along the zone boundaries. The primitive cell of cubic $Cs_2LiFeCl_6$ contains 10 atoms (2 Cs, 1 Li, 1 Fe, and 6 Cl), resulting in a total of $3N$ = 30 phonon modes. Among these, three are acoustic modes that start at zero frequency at the Γ-point and rise smoothly without turning negative, while the remaining 27 optical modes also stay fully positive across the entire Brillouin zone. The phonon density of states supports this observation, showing a normal and well-separated distribution of acoustic and optical vibrations without any unusual peaks or features that could indicate instability. Overall, these results confirm that the cubic phase of $Cs_2LiFeCl_6$ is mechanically and dynamically stable at 0 K, suggesting that it will

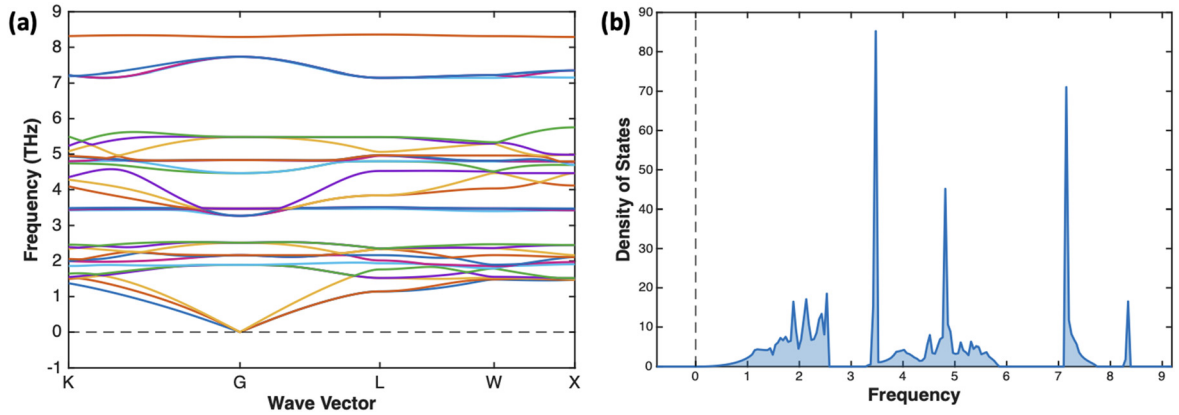

Fig. 2 Phonon band structure and total phonon density of states (TDOS) of the investigated material. (a) presents the phonon dispersion relationships along high-symmetry directions, while (b) shows the corresponding total DOS highlighting vibrational mode contributions.

maintain its structure without spontaneous distortions under normal conditions.

3.4 Mechanical properties

The mechanical properties of materials should be studied before their use in practical applications because many features of devices are the functions of the mechanical properties of materials that are used in their manufacturing. Therefore, materials, which exhibit the best mechanical properties, are of great importance for their implementation in numerous devices. The elastic constant links mathematically the mechanical and dynamical characteristics of materials and shows their reaction to external applied forces. Those properties of the proposed perovskite were determined by the strain-energy method, in which a range of small strains was applied to the lattice to deform the structure and the energy of the distorted phases was calculated, from which second-order elastic constants were predicted. The elastic response of the material with an applied strain can be determined by Hooke's law, and the Voigt notation is a straightforward way to express these responses:

$$\sigma_i = \sum_{j=1}^{6} C_{ij}\varepsilon_j \tag{6}$$

where both the stress (σ_i) and strain (ε_j) are represented by a matrix with six components and the second-order elastic stiffness tensor (C_{ij}) is expressed by a 6 × 6 matrix. The elasticity tensor of a cubic system is defined by three independent elastic constants, namely C_{11}, C_{12} and C_{44}. Mechanical stability can be determined by the Born stability criterion,[46] the following five constraints must be met to form a stable cubic phase:[47,48]

$$\begin{cases} C_{11} - C_{12} > 0 \\ C_{11} + 2C_{12} > 0 \\ C_{11} > 0 \\ C_{44} > 0 \\ C_{12} < B < C_{11} \end{cases} \tag{7}$$

The values obtained using the GGA approach are shown in Table 3 and thus the results confirm that the studied perovskite met the Born criterion which makes it mechanically stable. The resistance of a material to applied pressure can be assessed using the bulk modulus B. The magnitude of the bulk modulus determines the material's capacity to resist deformation, with higher bulk modulus indicating a more pronounced resistance to distortion caused by pressure. It is calculated using the formula:[49]

$$B = \frac{C_{11} + 2C_{12}}{3} \tag{8}$$

The shear modulus (G), was computed using the Voigt–Reuss approach.[50,51] The Voigt and Reuss methods for determining the moduli are given by:

$$G_V = \frac{C_{11} - C_{12} + 3C_{44}}{5} \tag{9}$$

$$G_R = \frac{5C_{44}(C_{11} - C_{12})}{4C_{44} + 3(C_{11} - C_{12})} \tag{10}$$

Table 3 Mechanical properties of selected double perovskites

Compound	C_{11} (GPa)	C_{12} (GPa)	C_{44} (GPa)	B (GPa)	G (GPa)	Y (GPa)	B/G	n	C_{12}–C_{44} (GPa)	Ref.
$Cs_2LiFeCl_6$	38.01	19.86	17.87	25.91	14.35	36.34	1.81	0.27	1.99	This work
$Cs_2AgFeCl_6$	34.80	16.86	11.71	22.84	10.53	27.37	2.17	0.30	5.15	52
$Cs_2NaGaBr_6$	38.97	14.16	14.52	22.80	13.64	34.10	1.65	0.25	−0.36	39
$Cs_2NaScCl_6$	30.83	0.38	8.22	9.91	10.40	23.11	0.95	0.11	−7.84	53
$Cs_2NaCrCl_6$	—	17.23	—	27.15	16.29	40.725	1.66	0.74	—	54
$Rb_2LiInCl_6$	29.66	17.16	12.88	21.33	9.64	25.12	2.21	0.30	4.28	55
Rb_2ScInI_6	36.825	8.230	4.505	17.762	7.313	19.292	2.429	0.319	3.725	56

$$G = \frac{G_V + G_R}{2} \quad (11)$$

From Table 3, it can be concluded that the bulk modulus of $Cs_2LiFeCl_6$ exhibits the strongest resistance to volume change when pressure is applied to it. In the same way, the shear modulus G relates to the material's response to shear stress, specifically as the ratio between shear stress and shear strain. The bulk modulus (B) is higher than the shear modulus (G), indicating that the material is more resistant to volume deformation than shape deformation. The magnitude of Young's modulus Y serves as an indication of the material's stiffness. The larger the Young's modulus, the less likely it is to deform and the stiffer the material is.

However, stiffness alone is not sufficient to evaluate the practical mechanical reliability of perovskite materials. Ductility is also an important factor because it reflects the ability of a material to accommodate mechanical strain without sudden fracture. This is particularly relevant for perovskite-based thin films, where stresses can develop during film deposition, device fabrication, substrate attachment, and thermal cycling. Previous studies on halide perovskites have shown that mechanical properties such as elasticity, hardness, and ductility are closely related to structural durability and fracture resistance.[57,58] In practical photovoltaic and optoelectronic devices, additional stresses may arise from thermal-expansion mismatch, interfacial strain, bending, and long-term operation. If the active material is highly brittle, such stresses can promote crack formation, interfacial degradation, and performance loss. Therefore, a ductile response is desirable because it can help the material tolerate mechanical deformation and maintain structural integrity during operation. This consideration is especially important for scalable thin-film fabrication and mechanically compliant device architectures, where strain tolerance is necessary for long-term device reliability.[59,60]

For comparison, the mechanical properties of structurally related halide double perovskites, including $Cs_2AgFeCl_6$, $Cs_2NaGaBr_6$, $Cs_2NaScCl_6$, and $Cs_2NaCrCl_6$, reported in earlier first-principles studies, are also summarized in Table 3. $Cs_2AgFeCl_6$ shows elastic constants and moduli of comparable magnitude to $Cs_2LiFeCl_6$, indicating a similar mechanical response under external stress. $Cs_2NaGaBr_6$ exhibits moderate bulk and shear moduli with a lower B/G ratio, suggesting comparatively reduced ductility. In contrast, $Cs_2NaScCl_6$ displays noticeably smaller elastic constants and bulk modulus, reflecting a mechanically softer lattice. $Cs_2NaCrCl_6$ presents relatively higher Young's and shear moduli among the referenced compounds, indicative of enhanced rigidity. Overall, $Cs_2LiFeCl_6$ demonstrates a balanced combination of stiffness, ductility, and mechanical stability when compared with these representative lead-free double perovskites.

Poisson's ratio[61] and Young's modulus[62] can be estimated by using the following relationships:

$$\nu = \frac{3B - E}{6B} \quad (12)$$

$$Y = \frac{9BG}{3B + G} \quad (13)$$

Pugh's ratio (B/G) and Poisson's ratio (ν) are important indicators of a material's ductility or brittleness. In Table 3, the Poisson's ratio (ν) value of our proposed perovskite is 0.27, while the Pugh's ratio (B/G) is 1.81. According to Pugh's criterion, a material is considered ductile if $\nu > 0.26$ and $B/G > 1.75$.[61] Based on these criteria, $Cs_2LiFeCl_6$ can be classified as ductile. Cauchy pressure (CP = $C_{12} - C_{44}$) can also be used to assess the bonding tendency, where a negative Cauchy pressure ($C_{12} - C_{44} < 0$) is generally associated with covalent-like bonding, while a positive Cauchy pressure ($C_{12} - C_{44} > 0$) suggests ionic-like bonding. The positive Cauchy pressure of $Cs_2LiFeCl_6$ indicates a predominantly ionic bonding tendency in the proposed perovskite.

Elastic anisotropy is related to the generation of microcracks; it also causes poor consistency in the results of tests reviewing the mechanical properties of materials. Therefore, the investigation of elastic anisotropy related to $Cs_2LiFeCl_6$ is favorable for better understanding the failure behaviors in these materials and, accordingly, improving their mechanical durability. When the anisotropy factor A is equal to 1, the compound behaves iso-tropically; otherwise, it behaves aniso-tropically, and if the anisotropy factor A is further away from 1, the anisotropy of the compound becomes more prominent.

We can determine the Zener anisotropy factor[63] A_z for these four compounds using their elastic constants, which can be calculated from the following equation:

$$A_z = \frac{2C_{44}}{C_{11} - C_{12}} \quad (14)$$

From Table 3, the calculated Zener anisotropy factor for $Cs_2LiFeCl_6$ is 1.97 which makes it moderately anisotropic. To facilitate a visual understanding of the anisotropic and elastic behavior of the investigated materials, three-dimensional (3D) plots were generated. These plots depict Young's modulus (Y), linear compressibility (β), shear modulus (G), and Poisson's ratio (ν) as shown in Fig. 3.

In this study, the anisotropy ratios Y_{max}/Y_{min},B_{max}/B_{min},G_{max}/G_{min} were used to quantify the degree of elastic anisotropy, where a larger ratio indicates stronger anisotropy, and the corresponding maximum and minimum values of bulk, shear, and Young's moduli along with their ratios are summarized in Table 4. The results showed that the 3D plot of Young's modulus was non-spherical as we can see from the table, the anisotropic ratio is 1.787, which makes this property anisotropic. For shear modulus and Poisson's ratio, the anisotropic ratio was found to be 1.969 and 26.971 thus we got the non-spherical figures. As for linear compressibility, it is a directional mechanical property derived from the elastic stiffness. The anisotropic ratio we found was 1.00 and it showed a spherical image because it depends only on the trace (bulk-like) response of the compliance tensor. It is a scalar function of direction and is less sensitive to shear or directional stiffness differences.

3.5 Electronic properties

The electronic structure of a material plays a pivotal role in determining its charge transport behavior, magnetic response,

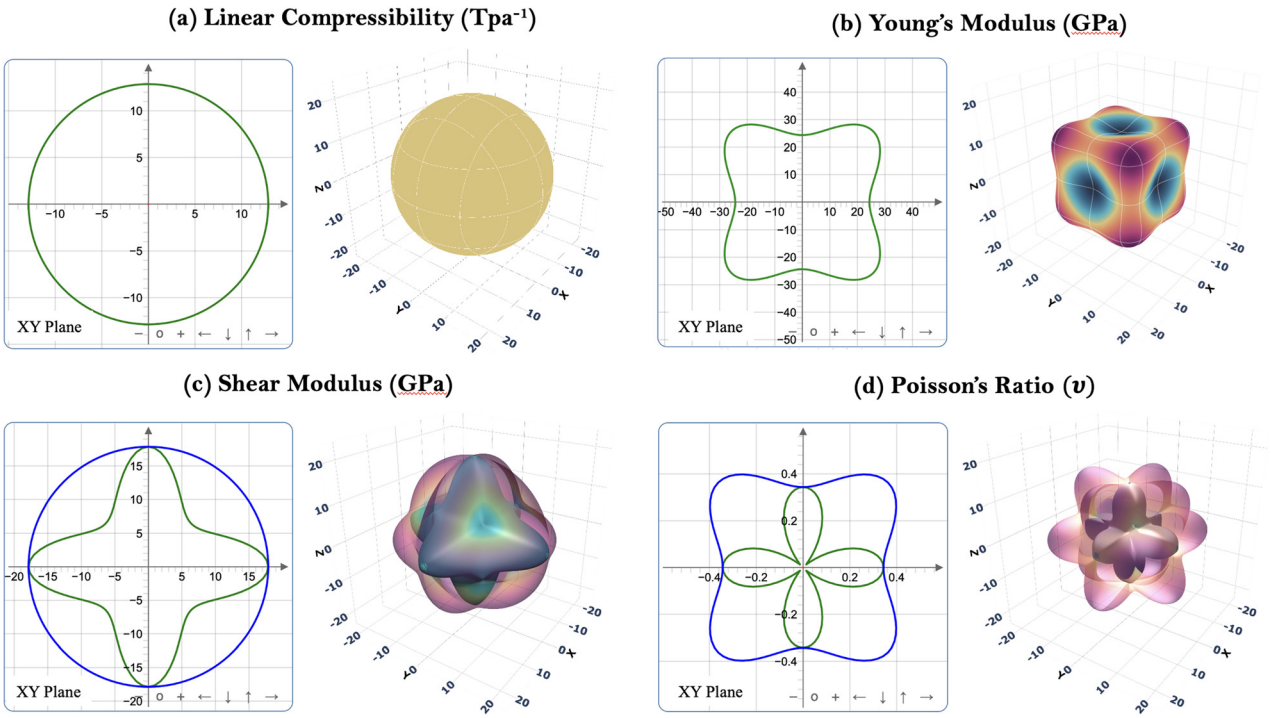

Fig. 3 Three-dimensional visualization of (a) linear compressibility (β), (b) Young's modulus (Y), (c) shear modulus (G), and (d) Poisson's ratio (ν) for the halide perovskite $Cs_2LiFeCl_6$.

and optoelectronic functionality, thereby providing fundamental insight into its underlying physical properties. A detailed understanding of the electronic band structure, along with the elemental and orbital contributions to the valence and conduction states, is crucial for evaluating the suitability of materials for optoelectronic and spin-dependent device applications, as well as for the rational engineering of their properties toward targeted functionalities. In this study, we systematically investigate the spin-polarized electronic band structure and density of states (DOS) of $Cs_2LiFeCl_6$. To accurately capture the localized and strongly correlated nature of the Fe 3d electrons, an on-site Hubbard U correction is further incorporated into the calculations.

3.5.1 Band structure. Fig. 4(a) and (b) present the calculated spin-resolved electronic band structures of $Cs_2LiFeCl_6$ obtained using the GGA and GGA+U approaches, respectively, along the high-symmetry paths of the Brillouin zone. Within the GGA framework, the spin-up channel exhibits a direct band gap of 4.446 eV, while the spin-down channel displays an indirect band gap of 1.138 eV. However, the overall band gap is markedly reduced to 0.470 eV due to the valence band maximum (VBM) originating from the spin-up channel and the conduction band minimum (CBM) derived from the spin-down channel. This artificial narrowing of the band gap stems from the intrinsic limitation of semilocal exchange–correlation functionals, which inadequately describe the localized nature of the Fe 3d electrons, resulting in a spurious overlap of Fe-derived states near the Fermi level.

Upon inclusion of the on-site Hubbard U correction for the Fe 3d orbitals, the electronic structure undergoes a pronounced modification. The improved localization of the Fe 3d electrons effectively eliminates the unphysical band overlap observed in the GGA results. As a result, the spin-up and spin-down band gaps increase to 5.107 eV and 1.578 eV, respectively, yielding a total band gap of 1.578 eV. The reported band gap of 1.578 eV was obtained from the GGA+U calculations. Although hybrid-functional methods such as HSE06 may further improve the quantitative accuracy of the band gap, the present GGA+U approach provides a physically reasonable description of the Fe-3d electronic structure and semiconducting behavior of $Cs_2LiFeCl_6$. Notably, within the GGA+U scheme, both the VBM and CBM are entirely contributed by the spin-down channel, signifying a transition from a mixed-spin band-edge configuration to a single-spin-dominated electronic structure. This behavior is consistent with previous studies on alkali-iron-based double perovskites, such as $Cs_2NaFeCl_6$, where the inclusion of a Hubbard U correction similarly restores the correct insulating ground state and spin-resolved band alignment.[17]

3.5.2 Density of states. To gain deeper insight into the electronic structure of $Cs_2LiFeCl_6$, the total density of states

Table 4 The anisotropic ratios, and maximum and minimum values of B, Y, G, and linear compressibility on the xy plane

Mechanical property	Min	Max	Anisotropic ratio
Bulk modulus B (GPa)	25.91	25.911	1.000
Young's modulus Y (GPa)	24.370	43.548	1.787
Shear modulus G (GPa)	9.073	17.868	1.969
Poisson's ratio ν	0.019	0.513	26.971
Linear compressibility β (TPa^{-1})	12.865	12.865	1.000

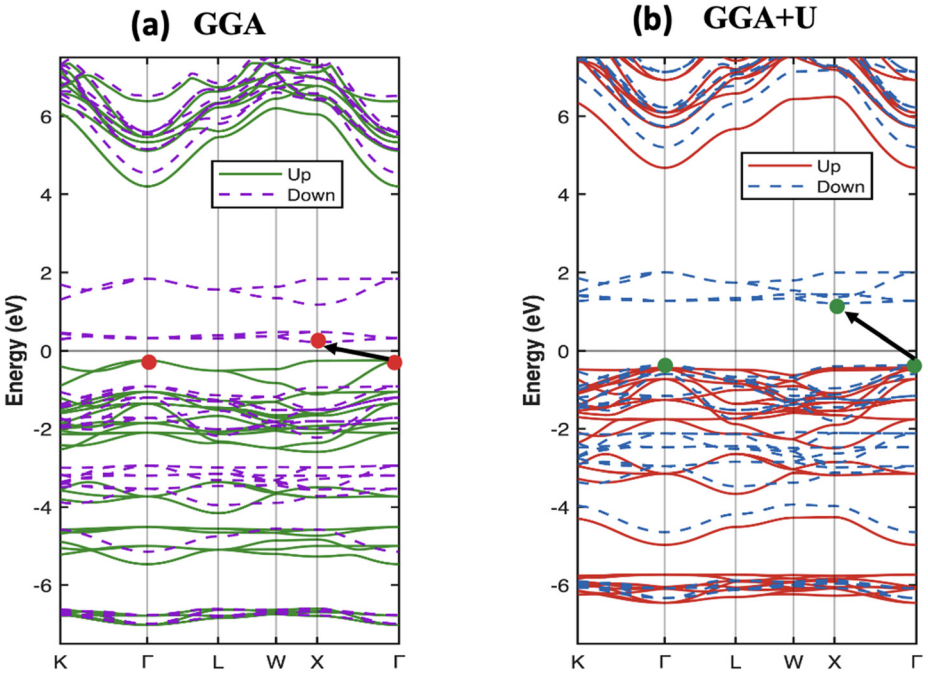

Fig. 4 Spin-resolved electronic band structures of $Cs_2LiFeCl_6$ calculated using the GGA approach: (a) without and (b) with the on-site Hubbard *U* correction applied to the Fe 3d states. The solid and dashed lines represent the spin-up and spin-down channels, respectively.

(TDOS) and projected density of states (PDOS) were analyzed, as shown in Fig. 5. The spin-resolved TDOS calculated within the GGA and GGA+*U* frameworks are presented in Fig. 5(a) and (e), respectively. In both cases, a clear separation between the

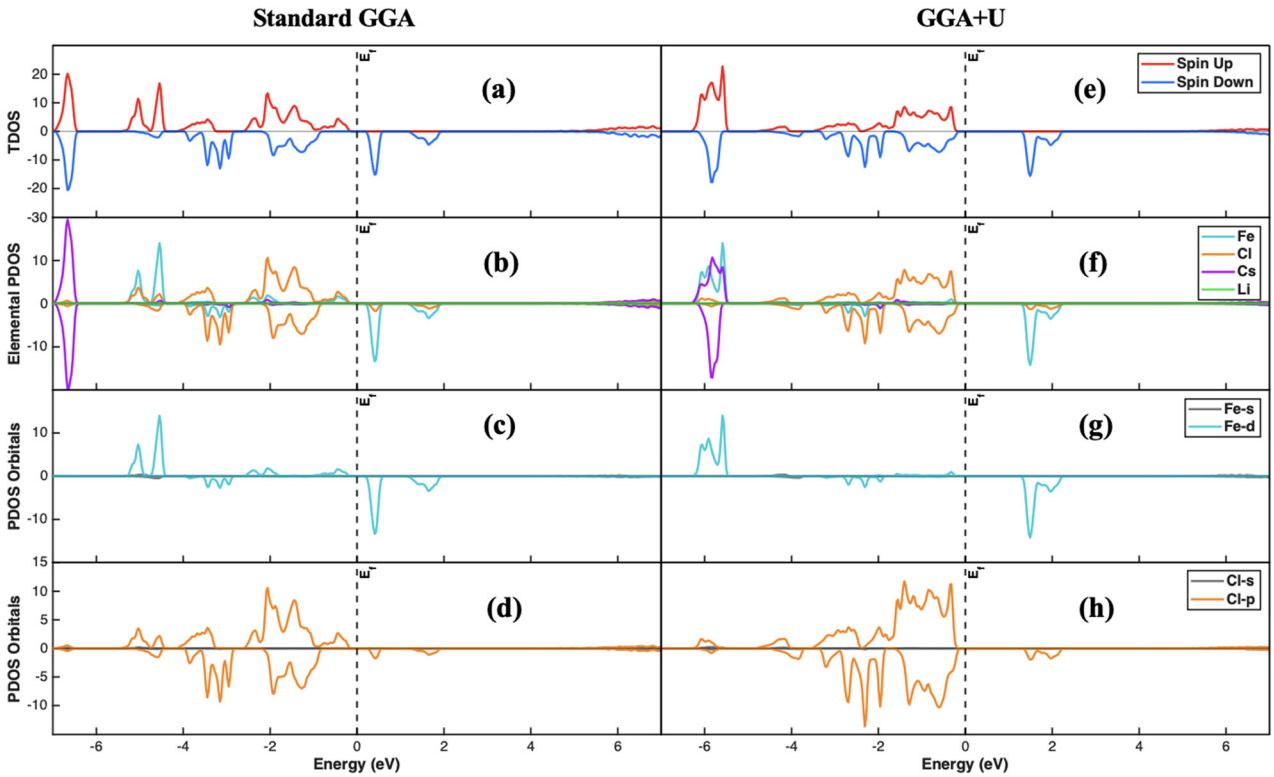

Fig. 5 Spin-resolved density of states (DOS) of $Cs_2LiFeCl_6$ calculated using the GGA approach. Panels (a)–(d) correspond to calculations without the Hubbard *U* correction, showing (a) total DOS, (b) elemental-projected DOS (PDOS), (c) orbital-projected DOS of Fe 3d states, and (d) orbital-projected DOS of Cl 3p states. Panels (e)–(h) present the corresponding results obtained with the on-site Hubbard *U* correction applied to the Fe 3d orbitals: (e) total DOS, (f) elemental PDOS, (g) orbital-projected DOS of Fe 3d states, and (h) orbital-projected DOS of Cl 3p states.

valence and conduction bands is observed, with no states crossing the Fermi level, confirming the semiconducting nature of the compound. A pronounced asymmetry between the spin-up and spin-down channels is evident, indicating an intrinsically spin-polarized electronic structure. This spin asymmetry originates from the combined effects of crystal-field splitting of the Fe 3d orbitals under octahedral coordination by Cl ligands and exchange interactions that lift the spin degeneracy of the Fe-derived states.

The element-resolved PDOS obtained using the GGA approach, shown in Fig. 5(b), reveals that the VBM in the spin-down channel is predominantly contributed by Cl states, whereas the spin-up VBM exhibits a mixed contribution from both Fe and Cl states. In contrast, the CBM in the spin-down channel is mainly derived from Fe states, with a smaller contribution from Cl. Further insight from the orbital-resolved PDOS of Fe 3d and Cl 3p states [Fig. 5(c) and (d)] indicates that the Cl contribution near both the VBM and CBM originates exclusively from Cl 3p orbitals, while the Fe contribution is governed by highly localized Fe 3d states. The strong covalent hybridization between Fe 3d and Cl 3p orbitals in the spin-up channel leads to an artificial upward shift of Fe-derived states toward the VBM, resulting in a spin-dependent band alignment and the formation of a spin-selective band gap within the GGA approximation.

Upon inclusion of the on-site Hubbard U correction, the electronic structure undergoes a significant modification, as reflected in the PDOS shown in Fig. 5(f)–(h). The element-resolved PDOS in Fig. 5(f) demonstrates a reduced contribution of Fe states near the Fermi level, indicating suppressed Fe 3d-Cl 3p covalent hybridization. As expected within the DFT+U framework, the occupied Fe 3d states are shifted toward lower energies, while the unoccupied Fe 3d states move to higher energies, as shown in Fig. 5(g), resulting in an overall widening of the band gap. Importantly, the application of U eliminates the spurious partial occupation of Fe-derived states near the Fermi level in the spin-up channel observed in the GGA results. Consequently, both the VBM and CBM are entirely confined to the spin-down channel, yielding a fully spin-polarized semiconducting ground state, as evidenced by the TDOS in Fig. 5(e).

To further clarify the bonding characteristics and charge distribution in $Cs_2LiFeCl_6$, electron localization function (ELF) analysis was performed, as shown in Fig. 6. Strong electron localization is observed around the Cl atoms, consistent with the dominant contribution of Cl-3p states near the valence-band region. In contrast, the Cs and Li regions exhibit relatively weak localization, confirming their predominantly ionic role in the elpasolite lattice. Partial electron localization is also observed within the Fe–Cl coordination environment, indicating finite Fe–Cl orbital interaction rather than purely ionic bonding. These results support a mixed ionic–covalent bonding character and provide real-space evidence for the Fe-3d/Cl-3p hybridization inferred from the PDOS analysis.

3.5.3 Carrier effective mass. The effective masses of charge carriers are key parameters governing the optoelectronic and photovoltaic performance of semiconducting materials, as they directly influence carrier mobility, charge separation efficiency,

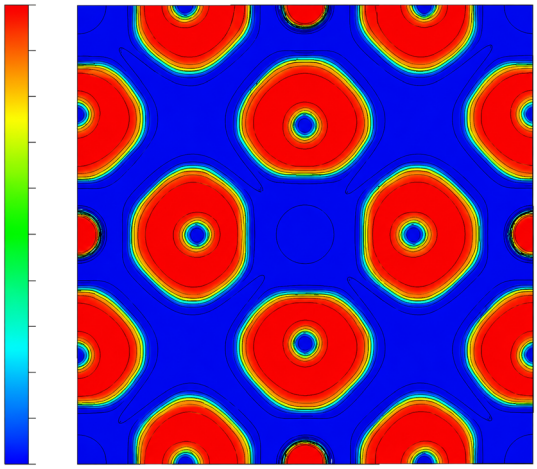

Fig. 6 Electron localization function (ELF) map of $Cs_2LiFeCl_6$ showing electron localization and mixed ionic–covalent Fe–Cl bonding characteristics.

and transport properties. In particular, carrier mobility is inversely proportional to the effective mass, as expressed in eqn (15). Consequently, materials with low carrier effective masses are highly desirable for efficient separation of photogenerated electron–hole pairs and for achieving high carrier mobility. Enhanced mobility enables charge carriers to reach reaction interfaces in photocatalytic processes or charge-collection layers in photovoltaic devices before recombination occurs.

In this study, the electron and hole effective masses were evaluated by fitting a second-order parabolic function to the electronic band dispersion in the vicinity of the band edges. Specifically, the effective masses were extracted using eqn (16) at the CBM and VBM. Within this formalism, steeper band curvature near the band edges corresponds to lower effective masses, whereas flatter dispersions indicate heavier carriers and reduced mobility:

$$\mu = \frac{e\tau}{m^*}, \tag{15}$$

$$\frac{1}{m^*} = \frac{1}{\hbar^2}\frac{\partial^2 E(k)}{\partial k^2}, \tag{16}$$

where $m^\star$ denotes the carrier effective mass, $\hbar$ is the reduced Planck constant, μ is the carrier mobility, e is the elementary charge, and τ represents the carrier relaxation time, which typically lies in the range of 10^{-13}–10^{-14} s for semiconducting materials.

The hole effective masses $\left(m_h^*\right)$ were calculated along the high-symmetry directions $\Gamma \rightarrow K$, $\Gamma \rightarrow L$, and $\Gamma \rightarrow X$, yielding values of $-0.923m_0$, $-1.127m_0$, and $-21.417m_0$, respectively. Similarly, the electron effective masses $\left(m_e^*\right)$ were evaluated along the $X \rightarrow W$ and $X \rightarrow \Gamma$ directions and were found to be $2.372m_0$ and $12.705m_0$, respectively. Notably, the electron effective masses are significantly larger than the hole effective masses, which is consistent with the electronic band structure, where the conduction band minimum exhibits a much flatter dispersion compared to the valence band maximum. The

pronounced ratio between the electron and hole effective masses (m_e^*/m_h^*) indicates a substantial asymmetry in carrier mobility. Such mobility disparity can be advantageous, as it promotes spatial separation of electrons and holes and effectively suppresses carrier recombination. As a result, this characteristic may enhance carrier lifetime, which is beneficial for photocatalytic reactions and photovoltaic charge extraction, despite the relatively reduced electron mobility associated with the heavy conduction-band states.

3.6 Optical and dielectric properties

In this study, we further investigated the frequency-dependent optical properties of the double perovskites to assess their capability in harnessing energy from electromagnetic radiation. Optical properties were evaluated by calculating the complex dielectric function,[64]

$$\varepsilon(\omega) = \varepsilon^1_{\alpha\beta}(\omega) + i\varepsilon^2_{\alpha\beta}(\omega) \tag{17}$$

The imaginary part of the dielectric function, $\varepsilon^2_{\alpha\beta}(\omega)$, can be found using the following equation:

$$\varepsilon^2_{\alpha\beta} = \frac{4\pi^2 e^2}{\Omega}\lim_{q\to 0}\frac{1}{q^2}\sum_{c,v,k} 2W_k\delta(\varepsilon_{ck} - \varepsilon_{vk} - \omega) \times \left\langle u_{ck+e_\alpha q}|u_{vk}\right\rangle\left\langle u_{ck+e_\beta q}|u_{vk}\right\rangle^* \tag{18}$$

The indices c and v represent the conduction band and valence band states, respectively. Here, u_{ck} denotes the cell periodic part of the orbitals at the k-point, while ω corresponds to the angular frequency of the electromagnetic (EM) radiation. Subsequently, the real part of the dielectric function[65] was derived using the Kramers–Kronig relationship, expressed as follows:

$$\varepsilon^1_{\alpha\beta}(\omega) = 1 + \frac{2}{\pi}P\int_0^\infty \frac{\varepsilon^2_{\alpha\beta}(\omega)'(\omega)}{\omega'^2 - (\omega)}\mathrm{d}\omega' \tag{19}$$

The remaining optical properties, such as the refractive index $n(\omega)$, extinction coefficient $k(\omega)$, energy loss function $L(\omega)$, absorption coefficient $\alpha(\omega)$, optical conductivity $\sigma(\omega)$, and reflectivity $R(\omega)$, can be calculated from the real and imaginary components of the dielectric function using the following equations:

$$n(\omega) + ik(\omega) = \frac{1}{\sqrt{2}}\left[\sqrt{\left\{\varepsilon^1_{\alpha\beta}(\omega)\right\}^2 + \left\{\varepsilon^2_{\alpha\beta}(\omega)\right\}^2} + \varepsilon^1_{\alpha\beta}(\omega)\right]^{1/2} \tag{20}$$

$$L(\omega) = \frac{\varepsilon^2_{\alpha\beta}(\omega)}{\left\{\varepsilon^1_{\alpha\beta}(\omega)\right\}^2 + \left\{\varepsilon^2_{\alpha\beta}(\omega)\right\}^2} \tag{21}$$

$$\alpha(\omega) = \sqrt{2}\omega\left[\sqrt{\left\{\varepsilon^1_{\alpha\beta}(\omega)\right\}^2 + \left\{\varepsilon^2_{\alpha\beta}(\omega)\right\}^2} - \varepsilon^1_{\alpha\beta}(\omega)\right]^{1/2} \tag{22}$$

$$\sigma(\omega) = -i\frac{2\omega}{4\pi}(\varepsilon(\omega) - 1) \tag{23}$$

$$R(\omega) = \left(\frac{\varepsilon_{\alpha\beta}(\omega) - 1}{\varepsilon_{\alpha\beta}(\omega) + 1}\right)^2 \tag{24}$$

3.6.1 Dielectric function. The dielectric function is a crucial parameter that influences charge carrier recombination rates and provides a clear understanding of optoelectronic device efficiency. Materials with higher static dielectric constants generally exhibit lower recombination rates, enhancing device performance. The real and imaginary components of the dielectric function, denoted as $\varepsilon_1(\omega)$ and $\varepsilon_2(\omega)$, respectively, play crucial roles in determining the material's response to external electromagnetic fields. The real part, $\varepsilon_1(\omega)$, characterizes the polarizability of the material, while the imaginary part, $\varepsilon_2(\omega)$, quantifies the energy dissipation within the medium.[66] Fig. 7a shows the real ($\varepsilon_1(\omega)$) and imaginary ($\varepsilon_2(\omega)$) components of the dielectric constant for $Cs_2LiFeCl_6$. The static dielectric constant $\varepsilon_1(0)$ is 4.33, consistent with its small bandgap, which is beneficial for reducing recombination and improving performance. As photon energy increases, $\varepsilon_1(\omega)$ rises to a peak near 5.98, then declines and eventually becomes negative which is shown in Fig. 7a. The negative values of $\varepsilon_1(\omega)$ signify regions where light transmission is forbidden, corresponding to strong plasmonic oscillations within the material.[67] The crossover to negative $\varepsilon_1(\omega)$ values occurs around 13.43 eV, which is defined as the plasma frequency. Above this energy, the material exhibits metallic-like behavior and strong plasmonic oscillations, leading to high reflectivity and blocking of higher-energy photons. This behavior demonstrates that $Cs_2LiFeCl_6$ acts as an efficient dielectric up to the plasma edge and serves as a strong UV-blocking material, making it promising for optoelectronic and UV coating applications. Additionally, these features indicate its potential as a solar cell absorber layer, where effective light harvesting and reduced carrier recombination are critical for achieving high conversion efficiency.

The imaginary part of the dielectric function, $\varepsilon_2(\omega)$, provides valuable insight into the electronic transitions between the valence and conduction bands and offers crucial information on optical absorption and energy dissipation mechanisms. By examining $\varepsilon_2(\omega)$, one can relate these transitions to the band structure of $Cs_2LiFeCl_6$. As depicted in Fig. 7A, the values of $\varepsilon_2(\omega)$ remain negligible at zero photon energy, confirming no optical absorption in this limit. In the infrared region (0.01–1.65 eV), $\varepsilon_2(\omega)$ remains nearly zero, indicating minimal absorption. In the visible range (1.65–3.1 eV), moderate peaks appear at 2.15 eV ($\varepsilon_2 \approx 2.42$) and 2.42 eV ($\varepsilon_2 \approx 3.40$), signifying good light harvesting abilities. In the UV region (>3.1 eV), strong peaks are observed, with a maximum value of approximately 4.57 at 8.15 eV, reflecting strong absorption. These peaks correspond to allowed transitions involving Fe-d and Cl-p orbitals, which dominate the conduction and valence band states, respectively. The precise energy positions and intensities highlight the interplay between electronic structure and optical

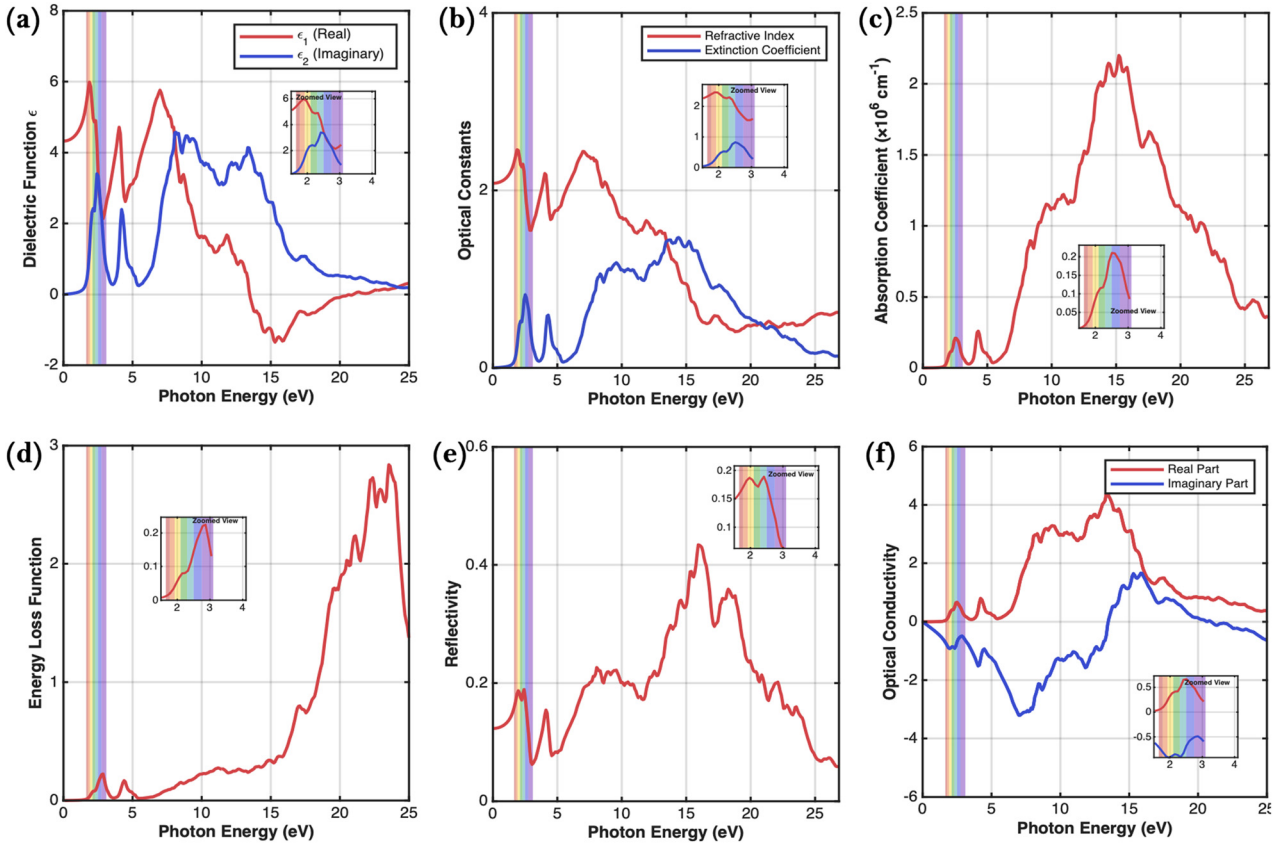

Fig. 7 Calculated optical properties of $Cs_2LiFeCl_6$. (a) Real and imaginary part of the dielectric function, (b) refractive index and extinction coefficient, (c) absorption coefficient, (d) energy loss function, (e) reflectivity, and (f) real and imaginary part of the optical conductivity.

properties, confirming the bandgap nature of this compound. The $\varepsilon_2(\omega)$ values represent the extent of light absorption and are directly proportional to the absorption coefficient $\alpha(\omega)$. Elevated $\varepsilon_2(\omega)$ values indicate strong light absorption, making $Cs_2LiFeCl_6$ particularly suitable for solar cell applications. Additionally, the observed peaks arise from interband and intraband electronic transitions between occupied and unoccupied states, providing valuable information about the conduction band landscape and the nature of electronic excitations.

3.6.2 Refractive index and extinction coefficient. The refractive index characterizes how light propagates through a material, a property that varies among different materials and plays a vital role in photonic and optical applications. Fig. 7B illustrates the variations in the refractive index $n(\omega)$. This parameter is directly related to the real part of the dielectric function, $\varepsilon_1(0)$, through the relationship $n(0) = \sqrt{\varepsilon_1(0)}$.[68] In this study, the static dielectric constant is determined to be $\varepsilon_1(0) = 4.33$, yielding a static refractive index of $n(0) = 2.08$, which lies within the expected range for wide bandgap semiconductors. The evolution of $\varepsilon_1(\omega)$ and $n(\omega)$ as functions of photon energy offers deeper insights into the dielectric properties of the material. As shown, $n(\omega)$ closely follows the behavior of $\varepsilon_1(\omega)$, with peak regions indicative of strong optical responses. Specifically, a maximum refractive index of 2.46 is observed at 1.88 eV, suggesting moderate light confinement capabilities in the visible spectrum. The moderate static and maximum refractive index values further confirm the material's potential for effective light dispersion and absorption, which are essential for optoelectronic and energy-harvesting applications.

The extinction coefficient, $k(\omega)$, measures the attenuation of electromagnetic radiation within the material and is directly linked to the imaginary part of the dielectric function, $\varepsilon_2(\omega)$. In this study, a peak value of 0.826 for $k(\omega)$ is recorded at 2.51 eV, with a corresponding ε_2 value of 3.34. These peaks in the $k(\omega)$ spectrum (Fig. 7b) are attributed to electronic transitions from occupied states in the valence band to unoccupied states in the conduction band, reflecting interband transitions that contribute to light absorption. However, when compared to highly absorbing materials such as $MAPbI_3$ or GaAs, which exhibit κ values exceeding 1.0 in the visible range,[69,70] the relatively low κ value observed here suggests limited intrinsic absorption. To achieve competitive photovoltaic performances, this may necessitate the incorporation of light-trapping strategies or thicker film designs.

These findings align with previous reports indicating that the refractive index and extinction coefficient serve as critical indicators of a material's optoelectronic suitability. Materials with higher n and κ values within the solar spectrum are particularly favorable for enhancing solar light absorption and promoting efficient photogenerated carrier generation.[71]

3.6.3 Absorption coefficient. Optical absorption is a key parameter for assessing the light-harvesting capability of semiconductor materials in optoelectronic, photovoltaic, and

photocatalytic applications, as it describes how effectively incident photons are absorbed as a function of photon energy.[72] In semiconductors, optical absorption mainly arises from electronic transitions from occupied valence-band states to unoccupied conduction-band states when the incident photon energy is sufficient to overcome the band gap. Therefore, the absorption coefficient is closely related to the electronic band structure and the imaginary part of the dielectric function.

Fig. 7c shows the calculated absorption coefficient, $\alpha(\omega)$, of $Cs_2LiFeCl_6$. The absorption spectrum starts to increase from approximately 0.09 eV, indicating the onset of low-energy optical transitions. The absorption remains relatively moderate in the infrared region, suggesting partial transparency at lower photon energies. However, it increases significantly upon entering the visible-light region. Notably, the absorption coefficient reaches approximately 1.63×10^4 cm^{-1} at 1.70 eV, which already exceeds the commonly used 10^4 cm^{-1} benchmark for efficient thin-film optical absorbers.[19,73] According to the Beer–Lambert absorption relationship,

$$A_{abs} = 1 - \exp(-\alpha d),$$

an absorption coefficient of 10^4 cm^{-1} corresponds to an optical penetration depth of approximately 1 μm, while approximately 80% absorption within a 1 μm-thick absorber requires $\alpha \approx 1.6 \times 10^4$ cm^{-1}. Thus, the calculated absorption at 1.70 eV indicates that $Cs_2LiFeCl_6$ can absorb a substantial fraction of visible photons within a device-relevant absorber thickness.

The visible-region absorption further strengthens with increasing photon energy and reaches approximately 2.10×10^5 cm^{-1} at 2.51 eV, confirming strong visible-light harvesting capability. A prominent absorption feature is observed around 4.12 eV, where α reaches 1.89×10^6 cm^{-1}. In the ultraviolet region, the absorption coefficient remains very high and exceeds 10^6 cm^{-1} beyond approximately 8 eV, indicating strong high-energy optical activity. Overall, the early absorption onset, visible-region absorption above the 10^4 cm^{-1} benchmark, and strong ultraviolet response suggest that $Cs_2LiFeCl_6$ is promising for solar-light-driven optoelectronic and photocatalytic applications.

3.6.4 Energy loss function. The electronic energy loss function (EELF) is a key parameter for studying optical properties across different energy regions. It is crucial for understanding momentum transfer, energy dissipation, and inelastic scattering. This function helps explain how a material responds to incoming energy and provides insight into its behavior across various energy ranges.

For $Cs_2LiFeCl_6$, Fig. 7d shows that the energy loss spectrum stays low and smooth in the visible range (1.7–3.2 eV). This suggests minimal energy loss and fewer electron scattering events, allowing strong light absorption and transmission without much damping. Such low loss is ideal for optoelectronic and photovoltaic devices. At higher energies, a strong plasmon peak appears around 23.54 eV (maximum value ~2.84), which is outside the visible range. The low energy loss in the visible spectrum highlights the material's promise for efficient light harvesting and minimal optical losses in solar and light-based applications.

3.6.5 Reflectivity. Optical reflectivity is pivotal for understanding electronic transitions between the valence and conduction bands in crystalline materials. Reflectivity measurements provide critical insight into how much light interacts with a semiconductor surface and are closely related to the material's absorption characteristics. In general, lower reflectivity values correspond to increased absorption of visible or ultraviolet light. Analyzing the relationship between reflectivity and absorption is essential for elucidating optical properties and assessing potential device applications. Fig. 7e illustrates the reflectivity behavior of $Cs_2LiFeCl_6$. The calculated reflectivity at zero photon energy is about 12.3%, indicating moderate reflection at low frequencies. In the infrared (0–1.7 eV), the average reflectivity is approximately 13.2%, suggesting partial transparency and low reflection losses. In the visible range (1.7–3.2 eV), the average reflectivity slightly increases to about 14.5% but notably drops below 10% around 2.86 eV. This decrease within the visible region implies enhanced light absorption and reduced surface reflection, which favor efficient light harvesting. These features make the material highly promising for optoelectronic and photovoltaic applications requiring strong absorption and minimal surface reflection.

3.6.6 Optical conductivity. Optical conductivity describes how a material responds to an external electromagnetic field and indicates its ability to support optical excitations. For $Cs_2LiFeCl_6$, the real part of the optical conductivity shows a maximum peak of about 4.42 at 13.43 eV, while the imaginary part reaches approximately 1.66 at 15.84 eV as shown in Fig. 7f. These strong peaks in the deep-UV region suggest efficient photon-induced electronic transitions and highlight the material's potential for high-energy optoelectronic applications. The significant optical activity at these energies indicates that $Cs_2LiFeCl_6$ could be a promising candidate for deep-UV photodetectors and other advanced photonic devices requiring strong absorption and fast carrier dynamics.

3.7 Green energy applications

3.7.1 Photocatalytic water splitting. Hydrogen is regarded as one of the cleanest energy sources, producing only water as a byproduct without emitting any toxic or greenhouse gases. However, industrial-scale hydrogen production primarily relies on carbon-intensive methods such as steam methane reforming, coal gasification, and partial oxidation of hydrocarbons. These processes utilize fossil fuels and coal, contributing significantly to carbon emissions and the release of greenhouse gases like CO_2, thereby undermining the environmental advantage of hydrogen fuel.

In contrast, photocatalytic water splitting offers an environmentally benign alternative, enabling hydrogen production directly from water using solar energy. This method harnesses photons from incident solar radiation to split water molecules without generating any carbon-based byproducts. The fundamental requirement for this process is a minimum energy input of 1.23 eV per electron transferred under standard

conditions.[74,75] For a material to be suitable for photocatalytic hydrogen evolution, its band-edge positions must be appropriately aligned with the water redox potentials. Specifically, the conduction band minimum (CBM) should be positioned at a more negative potential than the H^+/H_2 reduction potential, which corresponds to a higher electron energy on the vacuum energy scale. This energetic alignment enables photogenerated electrons in the CBM to reduce protons to H_2. Conversely, the valence band maximum (VBM) should be located at a more positive potential than the H_2O/O_2 oxidation potential, corresponding to a lower electron energy, so that photogenerated holes possess sufficient oxidizing power to drive water oxidation.[75,76] In the present work, the CBM and VBM positions were referenced to the vacuum level using surface slab calculations, enabling direct comparison with the pH-dependent water redox potentials. Moreover, an efficient photocatalyst should possess a suitable band gap for solar-light absorption, effective charge-carrier separation and transport, sufficient chemical and photostability, and active surface sites for proton reduction.[77,78] The incident photon must possess an energy greater than the band gap of the photocatalyst to excite an electron from the valence band to the conduction band, leaving behind a hole. These photogenerated electrons and holes subsequently participate in water-splitting redox reactions. Only under suitable energetic alignment can photocatalytic hydrogen evolution proceed thermodynamically.

Notably, the redox potentials of the hydrogen evolution reaction (HER) and oxygen evolution reaction (OER) are not fixed but depend on the pH of the aqueous medium. The pH-dependent expressions for these redox potentials are:[79]

$$E^{ox}_{O_2/H_2O} = -5.67 + 0.059\ \text{pH (eV)} \quad (25)$$

$$E^{red}_{H^+/H_2} = -4.44 + 0.059\ \text{pH (eV)} \quad (26)$$

In this analysis, the semiconductor band-edge positions referenced to the vacuum level are treated as fixed, while the aqueous redox potentials shift with pH according to the Nernst relationship. Therefore, the favorable photocatalytic pH range arises from the changing energetic alignment between the band edges and the redox potentials. Fig. 8(a) illustrates the pH-dependent variation of redox potentials, alongside the VBM and CBM energy levels of $Cs_2LiFeCl_6$. The analysis indicates that within a broad pH range of 2.70 to 8.61, the band edge positions of $Cs_2LiFeCl_6$ satisfy the energetic requirements for photocatalytic hydrogen evolution. Furthermore, $Cs_2LiFeCl_6$ possesses a significantly narrower bandgap (1.578 eV) compared to commonly used photocatalysts such as TiO_2 ($\sim$3.2 eV).[80] This allows it to harvest a wider portion of the solar spectrum, particularly the visible region, making it a more efficient candidate for solar-driven hydrogen production.

3.7.2 Carbon dioxide reduction. The rapid advancement of industrialization, rising global energy demand, and widespread deforestation have significantly accelerated the accumulation of carbon dioxide (CO_2) in the atmosphere. Nearly 40 to 42 gigatonnes of CO_2 are released annually, with a contribution of

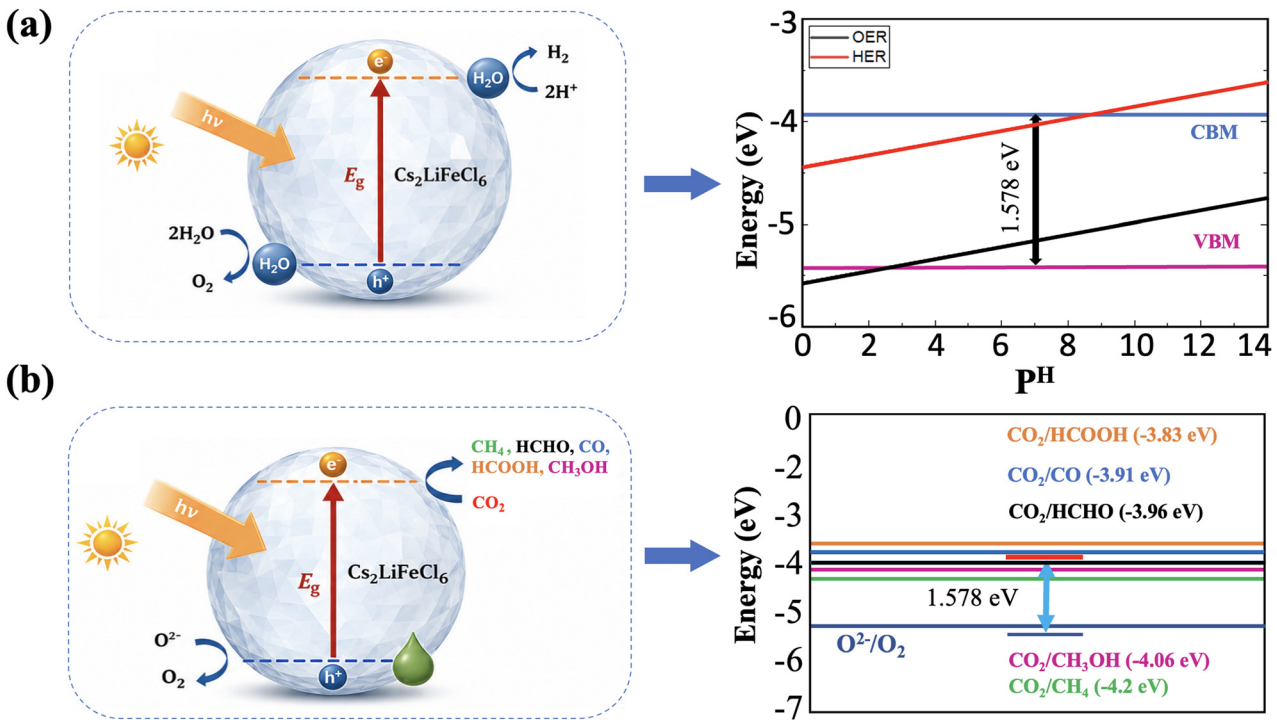

Fig. 8 (a) Schematic illustration of the photocatalytic hydrogen evolution mechanism on $Cs_2LiFeCl_6$ together with its calculated valence and conduction band edge positions referenced to the vacuum potential. (b) Schematic illustration of the photocatalytic carbon dioxide reduction mechanism on $Cs_2LiFeCl_6$ together with its calculated valence and conduction band edge positions referenced to the vacuum potential.

approximately 68% to global warming.[81] Photocatalysis has emerged as a promising route to mitigate CO_2 emissions by capturing and converting it into valuable products. An ideal photocatalyst can facilitate the solar driven reduction of CO_2 into carbonaceous fuels such as methane (CH_4), methanol (CH_3OH), formaldehyde (HCHO), and formic acid (HCOOH).[82]

The thermodynamic feasibility of CO_2 reduction is governed by the redox potential of each reaction, which depends on factors such as temperature, pH, and the target reduction product. In this work, the redox potentials of selected CO_2 reduction pathways at pH 7 were referenced to the absolute vacuum scale and compared with the calculated CBM of $Cs_2LiFeCl_6$ to evaluate the feasibility of photocatalytic reduction Fig. 8(b).

To drive these reduction reactions, the CBM of the photocatalyst should lie at a higher electron energy, *i.e.*, less negative on the absolute vacuum scale, than the redox potential of the desired CO_2 reduction product.[83] $Cs_2LiFeCl_6$ exhibits a CBM at −3.932 eV, which is positioned above the redox potentials for CH_3OH (−4.06 eV) and CH_4 (−4.20 eV), indicating that these reduction pathways are thermodynamically accessible based on band-edge alignment. The CBM is only slightly above the H_2CO formation potential (−3.96 eV), suggesting a very limited thermodynamic driving force for this pathway. In contrast, the redox potentials for HCOOH (−3.83 eV) and CO (−3.91 eV) lie above the CBM, making these pathways unfavorable under the same band-edge alignment criterion. Therefore, the present analysis should be regarded as a preliminary thermodynamic screening of photocatalytic CO_2 reduction feasibility based on band-edge alignment considerations.

In the context of CO_2 reduction, the selection of a suitable reducing agent is critical. Water (H_2O), hydrogen gas (H_2), and electrons are commonly used. While water is abundant and environmentally friendly, it can also lead to unintended hydrogen evolution rather than selective CO_2 reduction, especially when the CBM is positioned close to the HER potential.

Conclusions

In summary, first-principles density functional theory calculations establish the lead-free halide double perovskite $Cs_2LiFeCl_6$ as a structurally stable and multifunctional material for solar-energy-related applications. The compound stabilizes in the cubic $Fm\bar{3}m$ elpasolite structure with favorable tolerance factors, negative formation energy, positive decomposition energies, mechanical stability satisfying the Born criteria, and dynamic stability confirmed by phonon-dispersion analysis. Spin-polarized DFT+U calculations reveal a semiconducting band gap of 1.578 eV with spin-down-dominated band-edge states arising mainly from Fe-3d/Cl-3p orbital interactions, while the ELF analysis indicates a mixed ionic–covalent bonding characteristic within the $FeCl_6$ octahedral framework. The calculated effective masses suggest favorable electron–hole separation that may help suppress charge-carrier recombination. Furthermore, the optical properties demonstrate appreciable visible-light absorption, low reflectivity, and a strong optical response over a broad energy range, supporting efficient solar-photon harvesting. Band-edge alignment relative to the vacuum level further indicates that $Cs_2LiFeCl_6$ satisfies the energetic requirements for photocatalytic hydrogen evolution over a considerable pH range and shows favorable thermodynamic alignment for several photocatalytic CO_2 reduction half-reactions. These combined characteristics suggest that $Cs_2LiFeCl_6$ is a promising candidate for future lead-free photocatalytic and spin-dependent optoelectronic applications, while the present work provides a useful theoretical foundation for further experimental and advanced surface-level investigations of Fe-based halide double perovskites.

Author contributions

Md. Jahidul Islam and Mahbub Alam Rabin contributed equally to this work. Fahmida Gulshan supervised the study and contributed to the review and editing of the manuscript.

Conflicts of interest

There are no conflicts of interest to declare.

Data availability

All data supporting this study are available in the Zenodo repository: https://doi.org/10.5281/zenodo.18434642.

Acknowledgements

The authors are grateful to the Bangladesh University of Engineering and Technology (BUET) for providing the necessary research facilities and to the Committee for Advanced Studies and Research (CASR), BUET, for partial financial support. Additionally, we sincerely thank Dr Shaestagir Chowdhury for providing computational resources.

References

1 M. Di Sabatino, R. Hendawi and A. Sanchez Garcia, *Crystals*, 2024, **14**, 167.
2 S. Ghosh, H. Shankar and P. Kar, *Mater. Adv.*, 2022, **3**, 3742–3765.
3 M. A. Green, E. D. Dunlop, M. Yoshita, N. Kopidakis, K. Bothe, G. Siefer, D. Hinken, M. Rauer, J. Hohl-Ebinger and X. Hao, *Prog. Photovoltaics: Res. Appl.*, 2024, **32**, 425–441.
4 B. Tang, H. Dong, L. Sun, W. Zheng, Q. Wang, F. Sun, X. Jiang, A. Pan and L. Zhang, *ACS Nano*, 2017, **11**, 10681–10688.
5 X. Y. Chin, D. Cortecchia, J. Yin, A. Bruno and C. Soci, *Nat. Commun.*, 2015, **6**, 7383.
6 S. P. Senanayak, B. Yang, T. H. Thomas, N. Giesbrecht, W. Huang, E. Gann, B. Nair, K. Goedel, S. Guha, X. Moya,

C. R. McNeill, P. Docampo, A. Sadhanala, R. H. Friend and H. Sirringhaus, *Sci. Adv.*, 2017, **3**, e1601935.
7 S. Yakunin, M. Sytnyk, D. Kriegner, S. Shrestha, M. Richter, G. J. Matt, H. Azimi, C. J. Brabec, J. Stangl, M. V. Kovalenko and W. Heiss, *Nat. Photonics*, 2015, **9**, 444–449.
8 S. Park, W. J. Chang, C. W. Lee, S. Park, H. Y. Ahn and K. T. Nam, *Nat. Energy*, 2017, **2**, 16185.
9 B. W. Park and S. I. Seok, *Adv. Mater.*, 2019, **31**, 1900119.
10 D. B. Straus, S. Guo, M. M. Abeykoon and R. J. Cava, *Adv. Mater.*, 2020, **32**, 2001069.
11 Q. Zhang, F. Hao, J. Li, Y. Zhou, Y. Wei and H. Lin, *Sci. Technol. Adv. Mater.*, 2018, **19**, 425–442.
12 G. Volonakis, M. R. Filip, A. A. Haghighirad, N. Sakai, B. Wenger, H. J. Snaith and F. Giustino, *J. Phys. Chem. Lett.*, 2016, **7**, 1254–1259.
13 E. T. McClure, M. R. Ball, W. Windl and P. M. Woodward, *Chem. Mater.*, 2016, **28**, 1348–1354.
14 G. Niu, X. Guo and L. Wang, *J. Mater. Chem. A*, 2015, **3**, 8970–8980.
15 Z. Xiao, W. Meng, J. Wang, D. B. Mitzi and Y. Yan, *Phys. Rev. B*, 2017, **96**, 125201.
16 W. Li, N. U. Rahman, Y. Xian, H. Yin, Y. Bao, Y. Long, S. Yuan, Y. Zhang, Y. Yuan and J. Fan, *J. Semicond.*, 2021, **42**, 072202.
17 J. Klarbring, U. Singh, S. I. Simak and I. A. Abrikosov, *Phys. Rev. Mater.*, 2023, **7**, 044605.
18 G. Meyer and H.-C. Gaebell, *Z. Anorg. Allg. Chem.*, 1978, **445**, 117–132.
19 N. A. Noor, *et al.*, *J. Mater. Res. Technol.*, 2021, **13**, 2491–2500.
20 X. Zhou, J. Jankowska, H. Dong and O. V. Prezhdo, *J. Energy Chem.*, 2018, **27**, 637–649.
21 F. Aslam, H. Ullah and M. Hassan, *J. Mater. Sci. Eng. B*, 2021, **274**, 115456.
22 W. Shi, T. Cai, Z. Wang and O. Chen, *J. Chem. Phys.*, 2020, **153**, 141101.
23 J. Huang, H. Xiang, R. Ran, W. Zhou, W. Wang and Z. Shao, *Renewable Sustainable Energy Rev.*, 2024, **191**, 114187.
24 S. C. Yadav, A. Srivastava, V. Manjunath, A. Kanwade, R. S. Devan and P. M. Shirage, *Mater. Today Phys.*, 2022, **26**, 100731.
25 T. I. Alanazi, A. Shaker and D. Selim, *J. Alloys Compd.*, 2025, **1010**, 177354.
26 Z. Zhang, Q. Sun and Y. Lu, *et al.*, *Nat. Commun.*, 2022, **13**, 3397.
27 Y. Song, X. Li, H. Li, L. Wang, S. Xiao, H. Fei, G. Li and X. Song, *Appl. Catal., B*, 2025, **363**, 124816.
28 G. Wang, J. Wu, K. Deng, Q. Ding, W. Chi, Y. Tian and P.-P. Sun, *J. Catal.*, 2025, **449**, 116228.
29 Y. Tuo, C. Chen, Y. Xu, Z. Wang, Y. Du, Z. Han, X. Yun, S. Shi, J. Xie, S. Gao, W. Chen, C. Dong, X. Guan, G. Liu and P. Lu, *Phys. B*, 2025, **700**, 416942.
30 J. Pi, X. Jia, Z. Long, S. Yang, H. Wu, D. Zhou, Q. Wang, H. Zheng, Y. Yang, J. Zhang and J. Qiu, *Adv. Energy Mater.*, 2022, **12**, 2202074.
31 D. Wu, X. Liu, C. Tian, M. Zhou, Q. Huang and X. Tang, *iScience*, 2023, **26**, 107355.
32 M. Y. Khan, M. A. Jehangir, N. Israr, A. Hassan, U. Younis, J. Khane, M. Khane, A. Khan and A. Al Souwaileh, *Phys. B*, 2025, **707**, 417150.
33 H. Yin, Y. Xian, Y. Zhang, W. Chen, X. Wen, N. U. Rahman, Y. Long, B. Jia, J. Fan, W. Li and A. Heng, *Adv. Funct. Mater.*, 2020, **30**, 2002225.
34 Y. Zhou, A. M. Askar, J.-H. Pöhls, A. K. Iyer, A. O. Oliynyk, K. Shankar and A. Mar, *Z. Anorg. Allg. Chem.*, 2019, **645**, 323.
35 W. Li, N. U. Rahman, Y. Xian, H. X. Bao, Y. Long, S. Yuan, Y. Zhang, Y. Yuan and J. Fan, *J. Semicond.*, 2021, **42**, 072202.
36 X. Cao, L. Kang, S. Guo, M. Zhang, Z. Lin and J. Gao, *ACS Appl. Mater. Interfaces*, 2019, **11**, 38648.
37 C. J. Bartel, J. M. Clary, C. Sutton, D. Vigil-Fowler, B. R. Goldsmith, A. M. Holder and C. B. Musgrave, *J. Am. Chem. Soc.*, 2020, **142**, 5135.
38 F. Ji, J. Klarbring, B. Zhang, F. Wang, L. Wang, X. Miao, W. Ning, M. Zhang, X. Cai, B. Bakhit, M. Magnuson, X. Ren and L. Sun, *Adv. Opt. Mater.*, 2024, **12**, 2301102.
39 M. Younis Sofi, M. S. Khan, J. Ali and M. Khan, *Sci. Rep.*, 2024, **14**, 5520.
40 S. Das, A. Saha and S. K. Pradhan, *J. Mater. Res. Technol.*, 2021, **13**, 1460–1470.
41 S. S. Essaoud, *et al.*, *Chem. Phys. Lett.*, 2024, **835**, 141455.
42 P. Wisesa, K. A. McGill and T. Mueller, *Phys. Rev. B*, 2016, **93**, 155109.
43 C. Li, X. Lu, W. Ding, L. Feng, Y. Gao and Z. Guo, *Acta Crystallogr., Sect. B:Struct. Sci.*, 2008, **64**, 702–707.
44 C. J. Bartel, C. Sutton, B. R. Goldsmith, R. Ouyang, C. B. Musgrave, L. M. Ghiringhelli and M. Scheffler, *Sci. Adv.*, 2019, **5**, eaav0693.
45 R. D. Shannon, *Acta Crystallogr., Sect. A*, 1976, **32**, 751–767.
46 M. Born, *Math. Proc. Cambridge Philos. Soc.*, 1940, **36**, 160–172.
47 F. Mouhat and F.-X. Coudert, *Phys. Rev. B: Condens. Matter Mater. Phys.*, 2014, **90**, 224104.
48 B. B. Karki, G. J. Ackland and J. Crain, *J. Phys.: Condens. Matter*, 1997, **9**, 8579.
49 I. N. Frantsevich, *Elastic Constants and Elastic Moduli of Metals and Insulators*, Naukova Dumka, Kiev, 1982.
50 A. Reuss, *J. Appl. Math. Mech.*, 1929, **9**, 49–58.
51 R. Hill, *Proc. Phys. Soc., London, Sect. A*, 1952, **65**, 349–354.
52 K. Radja, B. L. Farah, A. Ibrahim, D. Lamia, I. Fatima, B. Nabil, A. Mohamed, Y. Al-Douri and A. Abd El-Rehim, *J. Phys. Chem. Solids*, 2022, **167**, 110795.
53 S. Shakeel, P. Song, S. H. Shah, Z. Zada, T. Huang, A. Laref, N. Hakimi and M. Faizan, *Mater. Chem. Phys.*, 2024, **324**, 129683.
54 J. Y. Al-Humaidi, A. Ullah, N. U. Khan, J. Iqbal, S. Khan, A. Algahtani, V. Tirth, T. Al-Mughanam, M. S. Refat and A. Zaman, *R. Soc. Chem.*, 2023, **13**, 20966–20974.
55 M. J. Islam, M. A. Rabin, K. M. Shahan and F. Gulshan, *Int. J. Hydrogen Energy*, 2026, **218**, 153749.
56 M. Y. Khan, M. A. Jehangir, I. E. Lee, Q. Wali, T. Usman, L. Xiaojie and A. Al Souwaileh, *Chem. Phys. Impact*, 2025, **11**, 100920.
57 S. Sun, Y. Fang, G. Kieslich, T. J. White and A. K. Cheetham, *J. Mater. Chem. A*, 2015, **3**, 18450–18455.

58 J. Feng, *APL Mater.*, 2014, **2**, 081801.
59 Z. Wang, Q. Lin, F. P. Chmiel, N. Sakai, L. M. Herz and H. J. Snaith, *Nat. Energy*, 2017, **2**, 17135.
60 Z. Li, T. R. Klein, D. H. Kim, M. Yang, J. J. Berry, M. F. A. M. van Hest and K. Zhu, *Nat. Rev. Mater.*, 2018, **3**, 18017.
61 G. Vaitheeswaran, V. Kanchana, A. Svane and A. Delin, *J. Phys.: Condens. Matter*, 2007, **19**, 326214.
62 M. Al-Fahdi, A. Rodriguez, T. Ouyang and M. Hu, *Crystals*, 2021, **11**, 783.
63 S. F. Pugh, *London, Edinburgh Dublin Philos. Mag. J. Sci.*, 1954, **45**, 823–843.
64 A. B. Siad, M. Baira, F. Z. Dahou, K. Bettir and M. E. A. Monir, *J. Solid State Chem.*, 2021, **303**, 122477.
65 M. Gajdoš, K. Hummer, G. Kresse, J. Furthmüller and F. Bechstedt, *Phys. Rev. B: Condens. Matter Mater. Phys.*, 2006, **73**, 045112.
66 Optical Properties of Materials and Their Applications, 2019.
67 H. Lashgari, A. Boochani, A. Shekaari, S. Solaymani, E. Sartipi and R. T. Mendi, *Appl. Surf. Sci.*, 2016, **369**, 76–81.
68 M. Fox and G. F. Bertsch, *Am. J. Phys.*, 2002, **70**, 1269.
69 G. E. Eperon, *et al.*, *J. Phys. Chem. Lett.*, 2017, **8**, 5864–5869.
70 I. Chung, *et al.*, *Nano Convergence*, 2016, **3**, 15.
71 Y. Ma, *et al.*, *RSC Adv.*, 2023, **13**, 25547–25554.
72 M. Fox, *Optical Properties of Solids*, Oxford University Press, Oxford, 2nd edn, 2010.
73 J. Nelson, *The Physics of Solar Cells*, Imperial College Press, London, United Kingdom, 2003.
74 D. Y. Heo, M. A. Tekalgne and S. Y. Kim, *EES Catal.*, 2024, **2**, 94–108.
75 T. Hisatomi, J. Kubota and K. Domen, *Chem. Soc. Rev.*, 2014, **43**, 7520–7535.
76 A. Fujishima and K. Honda, *Nature*, 1972, **238**, 37–38.
77 A. Kudo and Y. Miseki, *Chem. Soc. Rev.*, 2009, **38**, 253–278.
78 Q. Wang and K. Domen, *Chem. Rev.*, 2020, **120**, 919–985.
79 M. R. A. Kishore and P. Ravindran, *J. Phys. Chem. C*, 2017, **121**, 22216–22224.
80 Y. E. Tasisa, T. K. Sarma, R. Krishnaraj and S. Sarma, *Results Chem.*, 2024, **11**, 101850.
81 P. Friedlingstein, *et al.*, *Earth Syst. Sci. Data*, 2025, **17**, 965–1039.
82 J. Qiao, Y. Liu, F. Hong and J. Zhang, *Chem. Soc. Rev.*, 2014, **43**, 631–675.
83 F. Temerov, Y. Baghdadi, E. Rattner and S. Eslava, *ACS Appl. Energy Mater.*, 2022, **5**, 14605–14637.